

# Plastic deformation and fracture behaviour of Ti–6Al–4V alloy loaded with high strain rate under various temperatures

Woei-Shyan Lee \*, Chi-Feng Lin

*Department of Mechanical Engineering, National Cheng Kung University, Tainan 70101, Taiwan, ROC*

Received 8 November 1996; received in revised form 10 March 1997

## Abstract

This study investigates the plastic deformation and fracture behaviour of titanium alloy (Ti–6Al–4V) under high strain rates and various temperature conditions. Mechanical tests are performed at constant strain rates ranging from  $5 \times 10^2$  to  $3 \times 10^3 \text{ s}^{-1}$  at temperatures ranging from room temperature to 1100°C by means of the compressive split-Hopkinson bar technique. The material's dynamic stress–strain response, strain rate, temperature effects and possible deformation mechanisms are discussed. Furthermore, the plastic flow response of this material is described by a deformation constitutive equation incorporating the effects of temperature, strain rate, strain and work hardening rate. The simulated results based on this constitutive equation are verified. The fracture behaviour and variations of adiabatic shear band produced by deformation at each test condition are investigated with optical microscopy and scanning electron microscopy. The results show that the flow stress of Ti–6Al–4V alloy is sensitive to both temperature and strain rate. Nevertheless, the effect on flow stress of temperature is greater than that of strain rate. Fracture observations reveal that adiabatic shear banding turns out to be the major fracture mode when the material is deformed to large plastic strain at high temperature and high strain rate. © 1998 Elsevier Science S.A.

**Keywords:** Plastic deformation; Adiabatic shear fracture; Titanium alloys; High strain rates; Temperature sensitivity

## 1. Introduction

Ti–6Al–4V, an  $\alpha + \beta$  type titanium alloy, is of great importance in many industrial applications due to its highly attractive properties, such as good deformability, low density, high specific strength, excellent corrosion resistance and high temperature strength retention [1–3]. Since the mechanical characterization of Ti–6Al–4V is of great complexity and is strongly sensitive to the processing parameters, i.e. strain rate and temperature, it is important to clarify its deformation modes and the relationship between the processing variables, microstructure and properties under different loading conditions.

A number of quasi-static loading rate studies on this material have been carried out by means of various numerical, analytical and experimental methods, and their results have been published [4–7]. However, the data obtained for this material at high temperature and

with high strain rates is scanty. In fact, the high strain rate and high temperature properties of Ti–6Al–4V are most crucial in the design of structures and components subjected to impact or shock loading, which can lead to a drastic change in deformation modes and failure mechanisms. The conditions for which Ti–6Al–4V seems best suited are specifically the those which have not been adequately studied. Therefore, in order to obtain better insight into these problems, a systematic study of the effects of strain rate and temperature on the dynamic plastic deformation behaviour of Ti–6Al–4V alloy is required.

It is well recognized that strain rate, as well as temperature, affect many materials' properties including fracture initiation. A split-Hopkinson bar technique has been successfully developed to investigate the strain rate and temperature effects on the mechanical response of materials in the high strain rate regime [8]. Results obtained by Yadav and Ramesh [9] by this technique for two tungsten-based composites demonstrate that both composites display substantial increases in flow stress with increases in the applied strain rate

\* Corresponding author. Tel.: +886 6 2757575 ext. 62174; fax: +886 6 2352973.

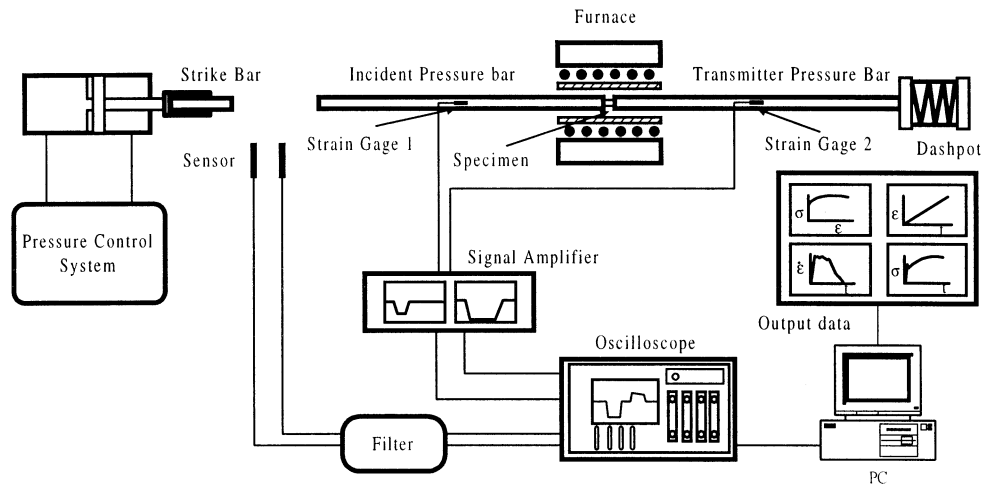


Fig. 1. Schematic presentation of the compression split-Hopkinson bar apparatus.

under a strain rate ranging from  $10^3$  to  $10^5 \text{ s}^{-1}$ . Chiem and Duffy [10] employed a torsional Hopkinson bar to study the dynamic flow behaviour and strain rate history effect on aluminum single crystal; they found a strong increase in strain rate sensitivity observed at strain rates exceeding  $500 \text{ s}^{-1}$ . More recently, Lee et al. [11,12] performed detailed investigations into the behaviour of AISI 4340 steel and tungsten composites undergoing deformation at dynamic rates and concluded that the higher the imposed strain rate, the greater the flow stress.

On the other hand, it is generally accepted that a rise of temperature tends to reduce the resistance of flow stress by lowering activation barriers associated with the atomic mechanisms of deformation. When a structural material is subjected to dynamic and high temperature loadings, a competing process between work hardening (resulting from the production, motion and interference of dislocations and other defects) and thermal softening occurs and affects the material's fundamental stress-strain behaviour. Extensive research into the temperature dependence of stress-strain curve parameters for many bcc and fcc metals have been carried out [13–15]. These experimental results show that at high temperature regimes, after work hardening to a peak stress, flow stress drops abruptly and then is followed by steady state behavior. These results also

show that temperature has proportionately a much greater effect on material strength than strain rate if the deformation is performed at both high strain rate and high temperature conditions.

The purpose of this paper is to present the influence of temperature and strain rate on the dynamic plastic deformation behaviour of Ti–6Al–4V alloy at strain rates ranging from  $5 \times 10^2$  to  $5 \times 10^3 \text{ s}^{-1}$  in the temperature range between room temperature and  $1100^\circ\text{C}$  using a compressive split-Hopkinson bar system. The formation of adiabatic shear bands and fracture features associated with different loading conditions are also described.

## 2. Experimental procedure

### 2.1. Material and specimens preparation

Hot-rolled commercial Ti–6Al–4V alloy bars, 15 mm in diameter and purchased from B and S Aircraft Alloys Inc., New York, were used in this investigation. Metallographic examination showed that the starting material had a structure characterized by final processing in the  $\alpha + \beta$  field. The chemical composition of the as-received bars is 6.1% Al, 4.0% V, 0.2% Fe, 0.014% C, 0.008% N, 0.0057% H, and 0.15% O. The cylindrical

Table 1  
Some mechanical characteristics of DC53 die steel bars

Density ( $\rho$ )	$7.87 \text{ g cm}^{-3}$
Young's modulus ( $E$ )	212.8 GPa
Shear modulus ( $G$ )	83.16 GPa
Poisson's ratio ( $\nu$ )	0.28
Wave velocity ( $C_0$ )	$5200 \text{ m s}^{-1}$
Yield stress ( $\sigma_y$ )	2880 MPa

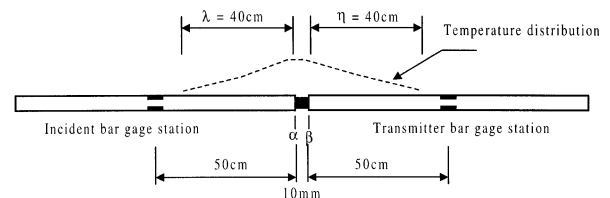


Fig. 2. Temperature distribution and strain gage stations of bars.

Table 2

Strain rate values obtained from different driving pressure, impact velocity and temperature conditions

Pressure (kg cm <sup>-2</sup> )	20	30	40	50	60	70	80
Impact velocity (m s <sup>-1</sup> )	35	42	49	54	60	65	72
Temperature (°C)							
25	—	400	450	800	1400	1700	2000
300	—	800	1400	1700	2000	2500	2700
500	750	1400	1700	2000	2500	—	—
700	800	1700	2000	2500	3300	—	—
900	1700	2000	2500	—	—	—	—
1100	2000	2500	—	—	—	—	—

specimens are all machined from the hot-rolled bar and turned to 10 mm in diameter and 10 mm in height in such a way that the compression axis is along the rolling direction. The actual dimensions reach an accuracy of 0.01 mm, as used in all our calculations.

## 2.2. Test procedures

Compression tests are carried out at constant strain rates ranging from  $5 \times 10^2$  to  $5 \times 10^3$  s<sup>-1</sup> at temperatures ranging from room temperature to 1100°C by means of a split-Hopkinson pressure bar. A schematic drawing of the apparatus is shown in Fig. 1, which is essentially the same as that described by Lindholm [16]. This system consists of incident and transmitter pressure bars on which SR-4 gages are installed to monitor the incident and transmitted pulses. The specimen is mounted between the incident and transmitter bars, with impact provided by a projectile propelled by a horizontal gas gun. The projectile, incident bar and transmitter bar are made from DC53 die steel with a diameter of 20 mm. The length of the incident and transmitted pressure bars is 1 m, while the striker bar (projectile) is 317 mm. Some mechanical characteristics

of DC53 die steel bars are presented in Table 1. To ensure the occurrence of fracture in the material by the first pulse during compression testing, an interrupting collar is placed around the specimen. For test temperatures below 300°C, the specimens are lubricated with a commercial molybdenum disulfide (Molykote). For temperatures ranging from 500 to 1100°C, a glass paste (80% PbO and 20% B<sub>2</sub>O<sub>3</sub> melted together and powdered with mortar and pestle, then mixed with alcohol) is used.

After the specimen assembly has been loaded into the induction furnace and aligned with the gun barrel, the furnace is put into operation and the specimen is heated up to the specified test temperature. The specimen temperature is regulated by a Eurotherm 211 programmer/controller connected to a Inconel sheathed chromel–alumel thermocouple, 1.5 mm diameter, attached to the specimen. The maximum temperature of a test sample is reached in about 10 min. The pressure bar ends extend into the furnace and thus are also heated. This heat is gradually distributed along the length of the bars, attaining an essentially steady-state temperature distribution along the pressure bars within 20 min. In order to measure the temperature distribution on the bars, additional thermocouples at intervals of 50 mm are cemented along the bars. The temperature distribution shows that the temperature, at 40 cm from the center, is only slightly above room temperature and therefore has a negligible effect on the nearest strain gage at 50 cm from the center. Because the thermal gradient not only affects the pulse reflections, but also changes the elastic modulus of the bars, calculations of specimen stress and strain must take the thermal gradient along the pressure bars into account when the specimen and adjacent portions of the pressure bars are heated.

Now, let  $\alpha$  denote the specimen interface with the incident bar and  $\beta$  the interface with the transmitter bar, while  $\lambda$  and  $\eta$  denote the temperature distributions in the incident and transmitter bars, respectively, as shown in Fig. 2. Under these circumstances, the displacement at the ends of the specimen is given by

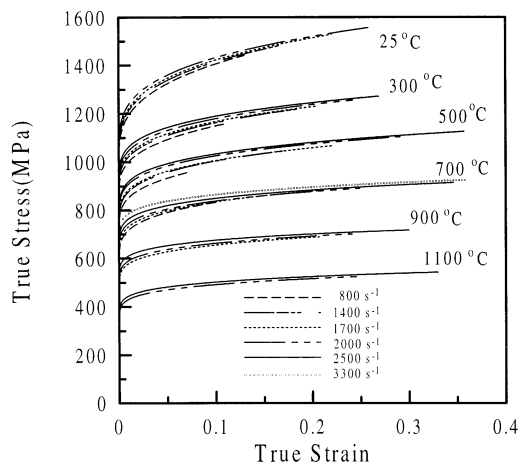


Fig. 3. Typical true stress–strain curves of Ti-6Al-4V alloy deformed at different strain rates and temperature conditions.

Table 3

Yielding strength ( $A$ ), material constant ( $B$ ), and work hardening coefficient ( $n$ ) of Ti–6Al–4V alloy deformed at different conditions

Temperature (°C)	Strain rate (s <sup>-1</sup> )	$A \sigma_y$ (MPa)	$B$ (material constant)	$n$ (work hardening coefficient)
25	400	970	1125.9	0.395
	450	982	1040	0.38
	800	998	850	0.32
	1400	1010	811	0.303
	1700	1017	801	0.298
	2000	1030	775.92	0.286
300	800	861	591	0.312
	1400	876	557.8	0.291
	1700	884	540	0.28
	2000	891	530	0.265
	2500	909	510	0.26
	2700	923	499	0.25
500	800	717.9	551	0.29
	1400	729	506.3	0.265
	1700	736.9	484.87	0.255
	2000	746	476.2	0.231
	2500	754	468.5	0.223
700	800	580	459.4	0.26
	1700	595	417.4	0.24
	2000	615	379	0.23
	2500	630	355.6	0.21
	3300	644	341	0.19
900	1700	470	313.5	0.23
	2000	480	298.5	0.215
	2500	495	278.5	0.19
1100	2000	330	255.7	0.2
	2500	343	245.7	0.19

$$u_\alpha = C_\alpha \int_0^t (2\epsilon_{I\alpha} - \epsilon_{T\beta} - 2\epsilon'_\alpha - \epsilon''_\beta) dt \quad (1)$$

$$u_\beta = C_\beta \int_0^t (\epsilon_{T\beta} - \epsilon''_\beta) dt \quad (2)$$

where  $C_\alpha = C_\beta$ , since the temperature is the same on both sides of the specimen.

If the length of the specimen is taken as  $L_0$ , then the nominal strain in the specimen is

$$\epsilon_s = \frac{(u_\alpha - u_\beta)}{L_0} \quad (3)$$

or in terms of the strain pulses

$$\epsilon_s = \frac{2C_\alpha}{L_0} \int_0^t (\epsilon_{I\alpha} - \epsilon_{T\beta} - \epsilon'_\alpha) dt \quad (4)$$

where  $\epsilon_{I\alpha}$  and  $\epsilon_{T\beta}$  are obtained from the strain pulses and, which are recorded at the incident and transmitter bar gage stations but corrected in amplitude according to the following relations. These relations compensate for pulse changes caused by transmission through the thermal gradient.

$$\frac{\epsilon_T}{\epsilon_I} = \frac{2E_1}{[E_2 + (E_1 E_2)^{1/2}]} \quad (5)$$

where  $E_1$  and  $E_2$  are the moduli of elasticity on the two sides of the thermal gradient of the bars and are

dependent on temperature.  $\epsilon'_\alpha$  is a reflection pulse which can be determined from  $\epsilon_{I\alpha}$  and  $\epsilon_{T\beta}$ . Eq. (4) is used to calculate specimen strain in high temperature ranges. The time in Eq. (4) is measured the instant that the incident strain pulse reaches the specimen. It can be seen that to determine the specimen strain, one does not need to obtain a record of the reflected pulse at the incident gage station.

The stress in the specimen is obtained from the strain at the face of the transmitter bar in contact with the specimen, that is  $\epsilon_{T\beta} + \epsilon''_\beta$ . Since this bar remains elastic, we have

$$\sigma_s = E_\beta (\epsilon_{T\beta} + \epsilon''_\beta) \quad (6)$$

where  $\epsilon''_\beta$  is a pulse which can be determined from  $\epsilon_{I\alpha}$  and  $\epsilon_{T\beta}$ .

In the case of room temperature tests, the following formulations are used to calculate the strain, strain rate and stress of the specimen.

$$\epsilon = \left( \frac{2C_0}{L_0} \right) \int_0^t \epsilon_r dt \quad (7)$$

$$\dot{\epsilon} = \frac{2C_0 \epsilon_r}{L_0} \quad (8)$$

$$\sigma = E \left( \frac{A}{A_0} \right) \epsilon_t \quad (9)$$

Table 4

Comparison of calculated and measured flow stress values at true strain of 0.1

Temperature (°C)	Strain rate (s <sup>-1</sup> )	$\sigma_{\text{meas}}$ (MPa)	$\sigma_{\text{cal}}$ (MPa)	$\sigma_{\text{cal}} - \sigma_{\text{meas}} / \sigma_{\text{meas}}$ (%)
25	800	1386.8	1404.8	1.3
	1400	1419.4	1413.7	-0.4
	1700	1394.8	1421.3	1.9
	2000	1406.2	1431.5	1.8
300	800	1155.0	1149.2	-0.5
	1400	1140.4	1162.1	1.9
	1700	1151.3	1167.4	1.4
	2000	1195.6	1178.9	-1.4
	2500	1171.7	1189.3	1.5
	2700	1170.3	1197.2	2.3
500	1400	977.7	1004.1	2.7
	1700	1028.0	1006.4	-2.1
	2000	1002.6	1025.7	2.3
	2500	1010.6	1033.8	2.3
700	800	814.6	832.5	2.2
	1700	813.2	835.2	2.7
	2000	849.2	838.16	-1.3
	2500	862.2	849.3	-1.5
	3300	887.3	864.2	-2.6
900	1700	645.6	654.6	1.4
	2000	645.8	661.9	2.5
	2500	668.8	674.8	0.9
1100	2000	504.9	491.3	-2.7
	2500	487.5	501.6	2.9
True strain = 0.1				Average = 0.81
				S.D. = 1.84

where  $C_0$  is the longitudinal wave velocity in the split-Hopkinson bar;  $L_0$  is the effective gage length of the specimen;  $E$  is the Young's modulus of the split bar;  $A$  and  $A_0$  are the cross-sectional areas of the split bar and the specimen, respectively.

### 2.3. Microstructural observations

After mechanical deformation, the microstructure is examined using optical and transmission electron microscopy (TEM) techniques. For optical microscopy, the specimens are sectioned on a Metaserve cut-off machine and then mounted in Metaserve DAP molding powder. After grinding with 400, 800 and 1200 grit paper, the specimens are polished with microcloth using a slurry of 0.3  $\mu\text{m}$  alumina and then etched in a solution of 2% HF, 10%  $\text{HNO}_3$  and 88%  $\text{H}_2\text{O}$  for 10 min. Finally, they are observed with MeF3 optical microscopy. For fractured specimens, features are studied using a JEOL JXA-840 scanning electron microscope operating at an acceleration potential of 20 Kv.

## 3. Results and discussion

### 3.1. Flow stress curve behavior and mechanical properties

The intensity of the dynamic load and the strain rate

in specimens is controlled by varying the impact velocity of the projectile. The strain rates listed in Table 2 are used for mechanical testing in order to compare the effects of both strain rate and temperature on the specimen's mechanical response. Under these strain rate and temperature conditions, the typical true stress-strain curves of Ti-6Al-4V are presented in Fig. 3. These curves are of the same kind and have a parabolic monotonic character with a pronounced loading maximum achieved before fracture. It is also clear that both the strain rate and temperature have obvious effects on the plastic deformation behaviour. Generally, flow stress increases with strain rate for a given temperature but decreases markedly with temperature if the specimen is deformed at a fixed strain rate. It should be noted here that although the flow stress shows a strong dependence on strain rate and temperature, the effect of the latter is more pronounced than that of the former. In addition, flow stress drops rapidly with temperature, indicating that dislocation annihilation is occurring far more rapidly than generation, and that the rate of thermal softening is much greater than that of work hardening during deformation, especially for the specimens deformed at temperatures higher than 500°C.

Actually, these stress-strain relations can be described suitably by a very simple model proposed by Ludwik [17] with the form of

$$\sigma = A + B \cdot \epsilon^n \quad (10)$$

Table 5  
Comparison of calculated and measured flow stress values at true strain of 0.2

Temperature (°C)	Strain rate (s <sup>-1</sup> )	$\sigma_{\text{meas}}$ (MPa)	$\sigma_{\text{cal}}$ (MPa)	$\sigma_{\text{cal}} - \sigma_{\text{meas}} / \sigma_{\text{meas}}$ (%)
25	1700	1533.7	1513.8	-1.3
	2000	1501.6	1519.6	1.2
300	1700	1229.3	1228.1	-0.1
	2000	1209.2	1237.0	2.3
	2500	1258.4	1244.6	-1.1
	2700	1273.0	1251.4	-1.7
500	1700	1056.4	1058.5	0.2
	2000	1101.7	1074.2	-2.5
	2500	1103.8	1080.6	-2.1
700	1700	869.1	878.7	1.1
	2000	863.7	876.7	1.5
	2500	881.8	883.6	0.2
	3300	907.9	895.2	-1.4
900	1700	702.7	686.5	-2.3
	2000	708.2	691.2	-2.4
	2500	683.0	700.1	2.5
1100	2000	507.7	515.3	1.5
	2500	526.6	524.0	-0.5
True strain = 0.2				Average = -0.27
				S.D. = 1.67

where  $A$  represents a constant, and is often yield strength.  $B$  is the material constant and  $n$  is the work hardening coefficient. Computed in accordance with this model, the variations of  $A$ ,  $B$  and  $n$  with strain rate and temperature are shown in Table 3. It is found that the yield strength increases with strain rate at temperatures ranging from 25 to 1100°C but decreases with temperature for a given strain rate. For material constant  $B$ , it is seen that a decrease of temperature or an increase of strain rate leads to a decrease in the material constant  $B$ . With regard to the work hardening coefficient,

$n$ , for all the strain rates and temperatures studied, the rate of work hardening decreases considerably as the testing temperature and strain rate increase. This result indicates that thermal softening always occurs at high temperature and at high strain rates and that deformation and interface friction cause the specimen temperature to increase. However, this rise of temperature leads to a dramatic reduction of the flow strength and the rate of work hardening.

In order to compare the accuracy of flow stress, as calculated by Ludwik's equation with that obtained

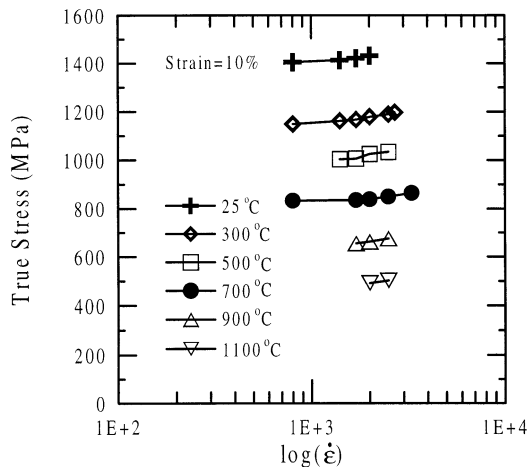


Fig. 4. Influence of strain rate on flow stress at a constant plastic strain of 10%, as a function of temperature.

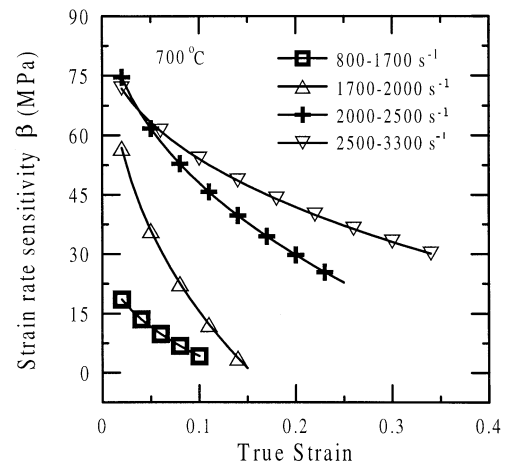


Fig. 5. Variations of strain rate sensitivity as a function of plastic strain for specimen deformed at 700°C under different strain rate ranges.

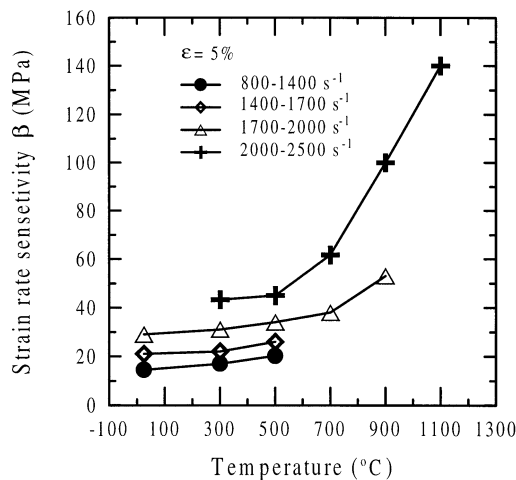


Fig. 6. Variations of strain rate sensitivity as a function of temperature for deformation at a true strain of 0.05 under different strain rate ranges.

from the experiments, a mean error of flow stress is defined as:

$$\text{percent error} = 100(\text{calculated stress} - \text{measured stress}) / \text{measured stress.} \quad (11)$$

Flow stress is calculated at a true strain of 0.1 and 0.2 using the Ludwik equation. An estimate of the consistency of this technique is obtained from the standard deviation. Table 4 and Table 5 list the results of this evaluation and show that the average error in the flow stress estimate is 0.81 and 0.27%, and the S.D. is 1.84 and 1.67% for true strains of 0.1 and 0.2, respectively. Although the calculated values agree quite well with the experimental ones, it should be noted that the latter are used for our subsequent mechanical characteristics analysis and data treatment.

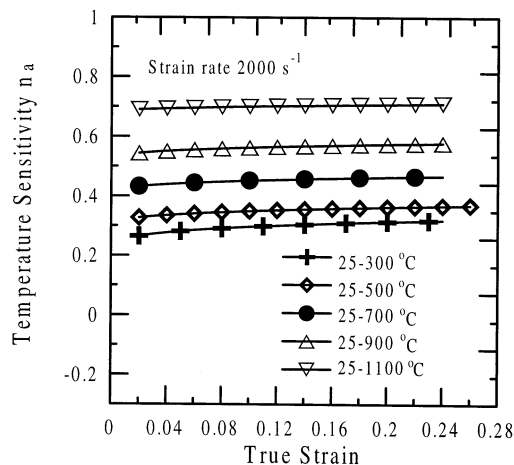


Fig. 7. Variations of temperature sensitivity as a function of plastic strain for a strain rate of  $2 \times 10^3 \text{ s}^{-1}$  under different temperature ranges.

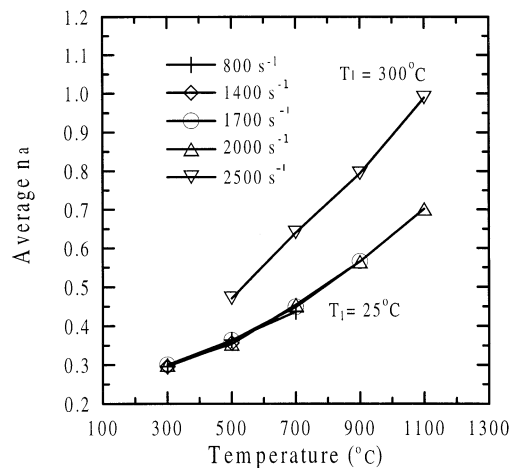


Fig. 8. Variations of temperature sensitivity as a function of temperature under different strain rates.

### 3.2. Effects of strain rate on flow stress

The influence of strain rate on flow stress at 10% fixed plastic strain is shown in Fig. 4, which presents the variations of flow stress at different temperatures with the logarithm of the mean strain rate. For each tested temperature, the strain rate sensitivity, as defined by the slope of the flow stress versus the log strain rate relationship, is almost constant. However, as seen in the comparison of temperature ranges, flow stress is quite sensitive to temperature but relatively less sensitive to strain rate. Typically, the macroscopic flow stress  $\sigma$  (compared at constant strain  $\epsilon$ ) varies linearly with strain rate, meaning that a thermally activated mechanism controls the deformation process. The same behavior has been observed for many materials [18–20], and their strength appears to increase dramatically when the strain rate is raised above  $10^3 \text{ s}^{-1}$  (or even  $10^4 \text{ s}^{-1}$ ). The work of Follansbee et al. [21] on pure polycrystalline copper showed that at a strain rate of around  $10^4 \text{ s}^{-1}$ , the mechanism controlling the rate of dislocation motion changed from thermal activation at the lower strain rate to viscous drag at the higher strain rate.

The plot of flow stress against the logarithm of strain rate, as mentioned above, can be utilized to obtain the strain rate sensitivity parameter  $\beta$ , defined as:

$$\beta = \frac{(\sigma_2 - \sigma_1)}{\ln(\dot{\epsilon}_2 / \dot{\epsilon}_1)} \quad (12)$$

where the compressive stresses  $\sigma_2$  and  $\sigma_1$  are obtained in tests conducted at the constant strain rates  $\dot{\epsilon}_2$  and  $\dot{\epsilon}_1$  respectively and are calculated at the same value of compressive plastic strain. Fig. 5 represents strain rate sensitivity as a function of true strain at different strain rate ranges for specimens tested at  $700^{\circ}\text{C}$ . When a specimen is deformed to a large strain value, the rate of

Table 6

Increase values of temperature for specimen deformed at strain rate of  $2 \times 10^3 \text{ s}^{-1}$  and strains ranging from 0.05 to 0.25 under six initial tested temperatures

Initial tested temperature (°C)	$\Delta T$ (°C)				
	$\epsilon = 0.05$	$\epsilon = 0.1$	$\epsilon = 0.15$	$\epsilon = 0.2$	$\epsilon = 0.25$
25	26.6	55.7	85.9	117.0	148.9
300	22.4	46.4	71.2	96.6	122.5
500	19.5	40.4	61.9	84.0	106.5
700	15.9	33.0	50.7	68.7	87.0
900	12.6	26.1	40.0	54.2	68.7
1100	9.3	19.3	29.6	40.2	50.0

thermal softening caused by temperature increase is greater than that of strain hardening induced by plastic deformation, and thus it can be seen that strain rate sensitivity decreases rapidly with true strain for all the strain rate ranges. In addition, at a fixed strain value, strain rate sensitivity increases with increasing strain rate range. A similar relationship between strain rate sensitivity and true strain are also found for our other tested temperatures. The dependence of strain rate sensitivity on temperature is also shown in Fig. 6, which indicates that strain rate sensitivity increases with temperature for four tested strain rate regions. Fig. 6 also indicates that the increase rate of strain rate sensitivity is more pronounced at high strain rates and high temperature.

### 3.3. Temperature sensitivity of flow stress

From the dynamic stress–strain curves in Fig. 3, it can be seen that temperature has considerable effect on the flow stress, especially at high temperature ranges. Based on these results, temperature sensitivity is expressed and calculated by a parameter  $n_a$ , defined as

$$n_a = \{\ln(\sigma_2/\sigma_1)\} / \{\ln(T_2/T_1)\} \quad (13)$$

where  $T_2 > T_1$ , and  $T_1 = 25^\circ\text{C}$ . Using the flow stress–strain data,  $n_a$  can be easily calculated by Eq. (13). Fig. 7 shows the variation of  $n_a$  with true strain for specimens deformed at a strain rate of  $2 \times 10^3 \text{ s}^{-1}$  under different temperature ranges. As can be seen from Fig. 7,  $n_a$  increases slightly with true strain for each incremental temperature range. However, at a fixed true strain value, it increases rapidly with temperature increment. On the basis of these results, it is clear that the effect of temperature on the variations of temperature sensitivity is more pronounced than that of true strain. This implies that during deformation, the rate of thermal softening dominates the flow stress behaviour and that the rate of strain hardening does not play a leading role in temperature sensitivity characteristics.

As mentioned above, temperature sensitivity has no obvious dependence on plastic true strain. For compari-

son purposes, we can neglect the effect of plastic true strain and take an average temperature sensitivity value for each temperature range under different strain rate conditions. Fig. 8 shows the average  $n_a$  as a function of temperature under five different strain rate conditions. It can be seen that for a given temperature range, under different strain rate conditions, the value of average  $n_a$  is about the same and appears to be independent of strain rate, which indicates that the average  $n_a$  does not change as strain rate increases. In addition, the higher the temperature, the more the average  $n_a$  increases. This implies that a considerable temperature sensitivity of flow stress exists, especially when the material is subjected to high temperature loading. It should also be noted that in Fig. 8, because flow stress–strain data for a strain rate of  $2.5 \times 10^3 \text{ s}^{-1}$  at room temperature is absent, a reference temperature of  $300^\circ\text{C}$  is chosen for calculation, and a similar relation between average  $n_a$  and temperature is obtained.

### 3.4. Deformation constitutive equation

Macroscopic results obtained in our study have shown that the plastic deformation behaviour of Ti–6Al–4V alloy depends strongly on strain rate and temperature. There are currently many different constitutive models available to describe the dynamic behaviour of materials with specific material constants [22–27]. One of the most common rate-dependent models, called the Johnson–Cook model [28], is used to describe the above mentioned deformation behavior. This model presents a constitutive equation for metals subjected to large strains, high strain rates and high temperatures and is expressed as

$$\sigma = (A + B\epsilon^n)(1 + c \ln \dot{\epsilon}^*) (1 - T^{*m}) \quad (14)$$

where  $\epsilon$  is the equivalent plastic strain;  $\dot{\epsilon}^* = \dot{\epsilon}/\dot{\epsilon}_0$  is the ratio of test strain rate to a reference strain rate, where we have chosen  $\dot{\epsilon} = 10^{-5} \text{ s}^{-1}$ ;  $T^*$  is the homologous temperature  $(T - T_{\text{room}})/(T_{\text{melt}} - T_{\text{room}})$ , and  $\sigma$  and  $\epsilon$  are stress and strain, respectively. The five material constants are  $A$ ,  $B$ ,  $n$ ,  $c$ , and  $m$ . The expression in the first



Table 7

Material parameters of Ti–6Al–4V alloy, AISI 4340 alloy and tungsten composite based on Johnson–Cook equation

Materials	$A$ (MPa)	$B$ (MPa)	$n$	$c$	$m$
Ti–6Al–4V	724.7	683.1	0.47	0.035	1.0
4340 Alloy	792	510	0.26	0.014	1.03
Tungsten composite	1093	1270	0.42	0.019	0.78

set of brackets gives stress as a function of strain with strain hardening coefficient  $B$  and strain hardening exponent  $n$ . The expression in the second and third sets of brackets represents the effects of strain rate and temperature, respectively.

The stress–strain curve data in the plot of Fig. 3 can be used to determine coefficients and exponents of the constitutive equation by a regression analysis technique which determines the best-fit parameters for all of the data for a given alloy. It should be noted that during plastic deformation, the work done in plastic flow is converted to heat which produces a rise in temperature in the specimen. Thus, the magnitude of temperature rise must be reckoned and a current temperature should be used to calculate the flow stress in our simulation model. At the presented test conditions, the temperature increase caused by the plastic work done,  $\Delta W$ , can be estimated by  $\Delta T = \Delta W / (\rho C_p)$ , where  $\Delta T$  is the increase in temperature,  $C_p$  is the specific heat ( $0.13 \text{ cal (g } ^\circ\text{C)}^{-1}$ ),  $\rho$  the density ( $4.43 \text{ g cm}^{-3}$ ) and  $\Delta W$  is the area under the stress–strain curve, which is given by  $\Delta W = \int_0^{\epsilon} \sigma_x \cdot d\epsilon_x$ . This calculation has been made for each of the tested temperature–strain-rate conditions. Table 6 lists the increase values of the temperature for specimens deformed at a strain rate of  $2 \times 10^3 \text{ s}^{-1}$  and strains of 0.05, 0.1, 0.15, 0.2 and 0.25 under six initial tested temperatures. According to the Johnson–Cook constitutive equation, and to replace the initial temperature with the current temperature for each interval of

strain in the regression process, the values of specific material parameters  $A$ ,  $B$ ,  $n$ ,  $c$ , and  $m$  for Ti–6Al–4V alloy are obtained and listed in Table 7, in which the ones for AISI 4340 alloy [29], and tungsten composites [9] evaluated by other investigators are also shown for comparison. By putting these five obtained material parameters into the Johnson–Cook constitutive equation, the deformation response of Ti–6Al–4V alloy under mathematical conditions equivalent to our actual experimental test conditions is predicted, and an example of the result corresponding to a strain rate of is shown in Fig. 9. Thus, we can conclude that the theoretical predictions do agree with the experimental result.

### 3.5. Fracture behaviour and microstructural observations on deformed specimens

After mechanical testing, scanning electron microscope studies were performed on the deformed specimens in an effort to identify fracture characteristics and mechanisms. We found that fracture occurred at an angle of  $45^\circ$  to the compression axis, was catastrophic and associated with adiabatic shear bands under strain rates higher than for all the tested temperatures. A specimen deformed at  $500^\circ\text{C}$  under a strain rate of  $2.5 \times 10^3 \text{ s}^{-1}$ , in Fig. 10a, is given as an example. In the top view of the sample as seen in Fig. 10b, an arc-shaped adiabatic shear band can be seen, while a flat shear band can be seen in the side view shown in Fig. 10c. All these observations show that there is a microstructural change in the shear bands. Traditionally, there are two types of adiabatic shear bands which can be distinguished: (a) transformed bands, in which a phase change occurs, and (b) deformed bands, which are characterized by a very high shear strain in a very thin zone of deformation. In our case, there is no doubt that the transformed band plays an important role in the fracture behaviour and is the predominant fracture feature of Ti–6Al–4V alloy.

From the observed fracture features, it is found that the rupture of specimens always occurs due to a separation along the adiabatic shear bands. Initially, voids are usually nucleated circularly or elliptically in the cross-section of the shear band. Then, generally, the voids are joined by severing of the separating ligaments. In Fig. 11, a typical array of coalesced voids in a well-devel-

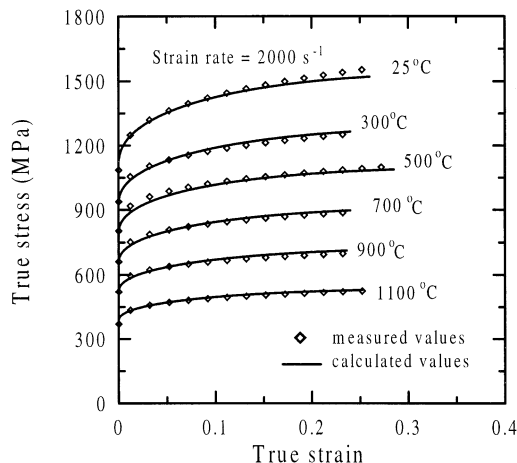


Fig. 9. Comparison between predicted and measured stress–strain curves for a strain rate of  $2 \times 10^3 \text{ s}^{-1}$ .

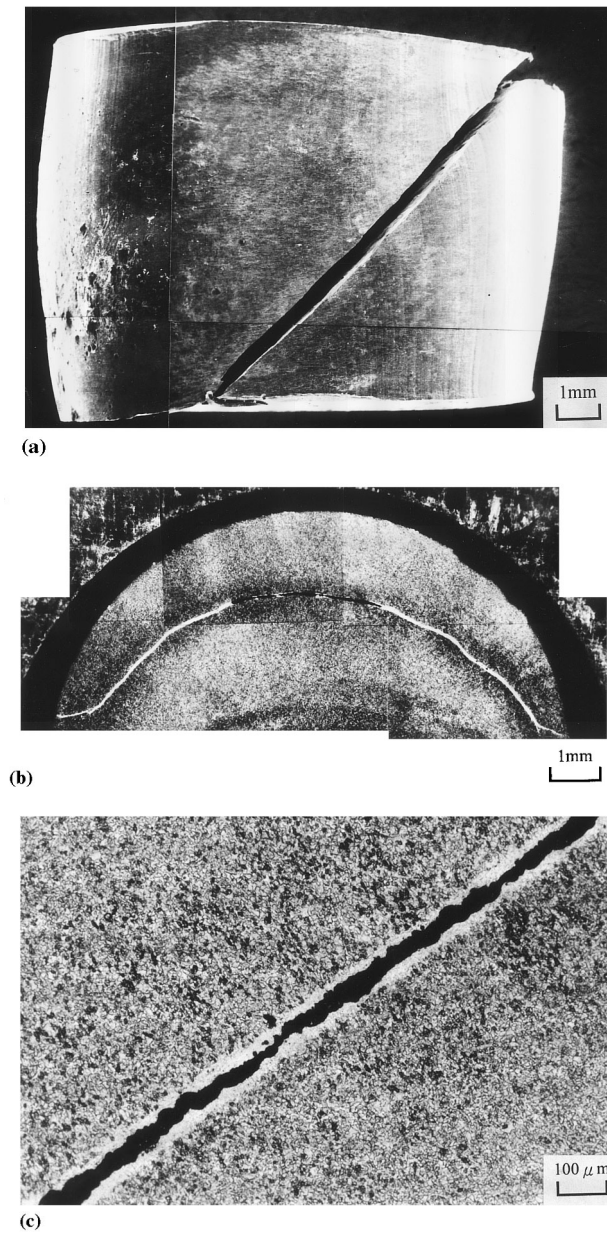


Fig. 10. a. Scanning electron micrographs of the specimen after fracture at 500°C and at  $2.5 \times 10^3 \text{ s}^{-1}$ , showing typical adiabatic shear failure. b. Top view by optical microscopy of the specimen after fracture at 500°C and  $2 \times 10^3 \text{ s}^{-1}$ , showing arc type of adiabatic shear band. c. Side view by optical microscopy of the specimen after fracture at 500°C and  $2 \times 10^3 \text{ s}^{-1}$ , showing planar type of adiabatic shear band.

oped shear band is shown. The diameters of the voids and the widths of the cracks are always less than those of the shear band from which they formed. Our observations also demonstrate that the fracture sites can be microvoids nucleated either at weak points in the adiabatic shear zone, or at sections of the shear surfaces where significant thermal softening is undergone.

In order to describe the fracture mechanisms operating in this material, a schematic of the observed frac-

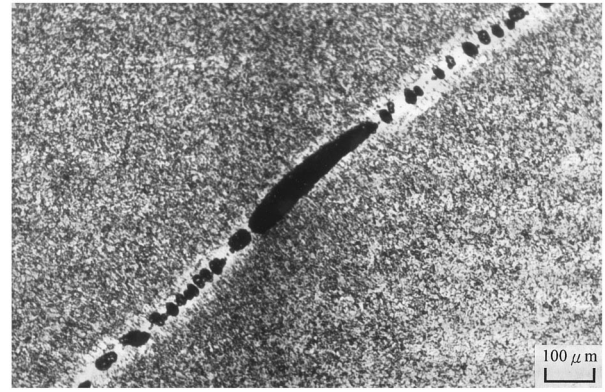


Fig. 11. Voids and cracks in an adiabatic shear band for the specimen deformed at 700°C under  $2 \times 10^3 \text{ s}^{-1}$ .

ture features and the orientation of the adiabatic shear band is shown in Fig. 12. In the separated fracture surface, two regions, called the shear zone and the tension zone, are indicated. It is known that in uniaxial compression, bands of localized deformation occur on planes of maximum shear stress oriented at  $45^\circ$  to the axis of compression. However, when there is a bulge on the specimen, a hoop stress appears at the equatorial plane of the cylindrical surface which induces a tensile loading state. Therefore, the shear zone and tension zone coexist in the shear band and form an X in the fracture plane. Besides, it is generally recognized that quickly loading most materials under high strain rate deformation will cause a dramatic rise of temperature. This rise in temperature will then cause thermal softening and transform the deformation from a homogeneous state to a heterogeneous state characterized by a distribution of localized shear bands. Thus, we can say that the formation and propagation of an adiabatic shear band is the favourite mode of failure for this material.

It is interesting to note that adiabatic shear behavior can also be found in the specimen tested above the  $\beta$ -transus temperature, i.e. 997.5°C. This phenomenon

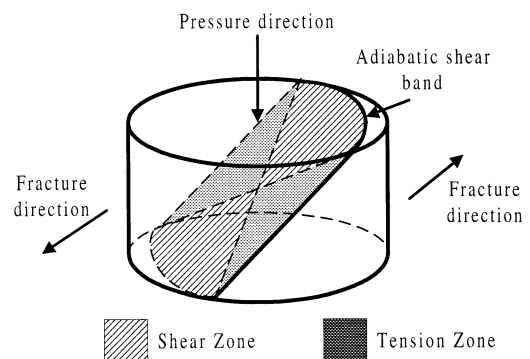


Fig. 12. Schematic description of fracture features and orientation of adiabatic shear band.

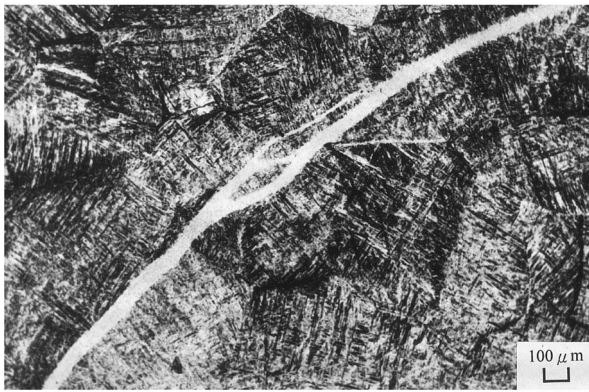


Fig. 13. Optical micrograph of adiabatic shear band obtained from the specimen tested at 1100°C under  $2 \times 10^3 \text{ s}^{-1}$ .

is clearly seen in Fig. 13, which corresponds to a specimen deformed at 1100°C and  $2.5 \times 10^3 \text{ s}^{-1}$ . When the tested temperature exceeds the  $\beta$ -transus temperature, there is a dramatic change in matrix structure, i.e. from  $\alpha + \beta$  phase to a single phase of  $\beta$ . Although the adiabatic shear band features both below and above the transus temperature are similar to each other, there is a large difference in the hardness and thickness of the shear bands (see Fig. 14). In other words, the hardness of the adiabatic shear band obtained from the specimen tested below transus temperature, 450 Hv, is much greater than that of above, i.e. 395 Hv. In addition, in both cases, the hardness reaches its maximum at the center of the shear band, then dramatically decreases to matrix hardness at the two sides. Moreover, the hardness in the right side of shear band is higher than that

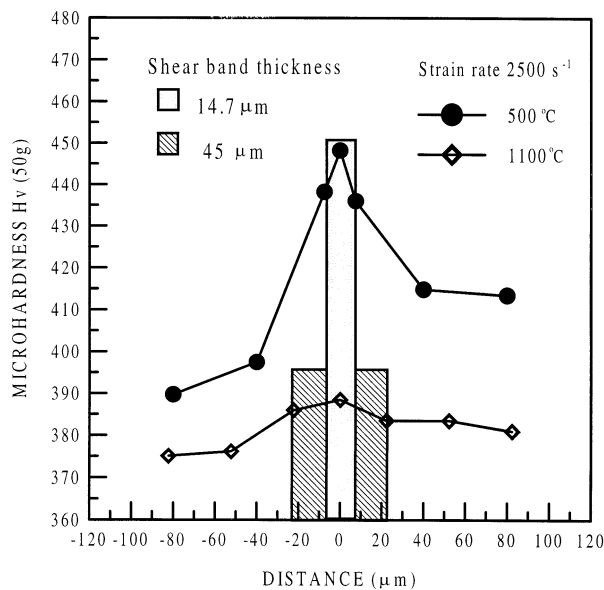


Fig. 14. Change in microhardness of adiabatic shear band for specimens tested at strain rate of, at both 500°C and 1100°C.

of left side. This can be explained by the fact that the deformation between the shear band and equatorial plane of the cylindrical surface is larger than that of the central region of specimen.

It is also noticeable that the thickness of adiabatic shear band is dependent upon the transus temperature. For example, under a strain rate of  $2.5 \times 10^3 \text{ s}^{-1}$ , the thickness of the adiabatic shear band increases from 14.7 μm at 500°C to 45 μm at 1100°C. This indicates that formation and growth of the adiabatic shear band are more active in the  $\beta$  phase than in the  $\alpha + \beta$  phase and that all microstructural variants in the adiabatic shear band are very sensitive to transus temperature. Also, the thickness of the adiabatic shear band decreases fairly rapidly with tested temperature, indicating that deformation becomes more difficult for specimens tested below the transus temperature.

#### 4. Conclusions

The plastic deformation behaviour of Ti–6Al–4V alloy subjected to high strain rate under various temperature conditions has been reported. Results obtained from mechanical testing show that flow stress, material constants and work hardening coefficient are sensitive to strain rate and temperature. Evaluation of temperature effects shows that temperature sensitivity increases with the increase of temperature, but is independent of strain rate. By using our experimentally determined specific material parameters in our proposed constitutive equation, a fairly good agreement with the experimental results is seen. Fracture observations reveal that the adiabatic shear bands are the precursor to crack formation and fracture. Hardness and thickness of the adiabatic shear bands are found to change directly with the transus temperature. An increase of temperature results in a decrease of the microhardness of the shear bands, but the thickness of the shear bands is found to increase with temperature.

#### References

- [1] R.A. Wood, Titanium Alloy Handbook, Metals and Ceramics Information Center, Battelle, Publication No. MCIC-HB-02, December 1972.
- [2] E.W. Collings, J.C. Ho, Physical properties of titanium alloy, in the science, technology and application of titanium, in: R.I. Jaffee, N.E. Promisel (Eds.), Proc. First Int. Conf. on Titanium, London, Pergamon Press, Oxford, 1970, p. 331.
- [3] M.K. McQuillan, Metall. Rev. 8 (1963) 41.
- [4] C.C. Chen, J.E. Coyne, Metall. Trans. A 7A (1976) 1931.
- [5] P.S. Follansbee, G.T. Gray III, Metall. Trans. A 20A (1989) 863.
- [6] S.V. Kailas, Y.V.R.K. Prasad, S.K. Biswas, Metall. Mater. Trans. A 25A (1994) 2173.
- [7] M. Mier, A.K. Mukherjee, Scripta Metall. Mater. 24 (1990) 331.
- [8] H. Kolsky, Proc. Phys. Soc., London, Sect. B 62 (1949) 676.

- [9] S. Yadav, K.T. Ramesh, *Mater. Sci. Eng.* A203 (1995) 140.
- [10] C.Y. Chiem, J. Duffy, *Mater. Sci. Eng.* 57 (1983) 233.
- [11] W.S. Lee, H.F. Lam, *J. Mater. Process. Technol.* 57 (1996) 233.
- [12] W.S. Lee, S.T. Chiou, *Composites: Part B* 27B (1996) 193.
- [13] L.X. Zhou, T.N. Baker, *Mater. Sci. Eng.* A177 (1994) 1–9.
- [14] T. Sakai, M. Ohashi, K. Chiba, *Acta Metall.* 36 (1988) 1781.
- [15] L. Blaz, T. Sakai, J.J. Jonas, *Met. Sci.* 17 (1983) 609.
- [16] U.S. Lindholm, *J. Mech. Phys. Solids* 12 (1964) 317.
- [17] P. Ludwik, *Elemente der technologischen Mechauik*, Springer, Berlin, 1909.
- [18] J. Adamczyk, M. Carsi, R. Kozik, R. Wusatowski, *J. Mater. Process. Technol.* 53 (1995) 15.
- [19] T. Mukai, K. Ishikawa, K. Higashi, *Mater. Sci. Eng.* A204 (1995) 12.
- [20] T. Nicholas, Material behaviour at high strain rates, in: J. Zukas et al. (Eds.) *Impact Dynamics*, Wiley, New York, 1982, 277.
- [21] P.S. Follansbee, G. Regazzoni, U.F. Kocks, *Mechanical Properties of Materials at High Rates of Strain*, Inst. Phys. Conf. Ser. 70, Institute Physics, London, 1984, p. 71.
- [22] F.J. Zerilli, R.W. Armstrong, AD-vol. 48, *High Strain Rate Effects on Polymer, Metal and Ceramic Matrix Composites and Other Advanced Materials* ASME, (1995) 121.
- [23] M. Zhou, R.J. Clifton, A. Needleman, *J. Mech. Phys. Sol.* 42 (1994) 423.
- [24] V. Ramachandran, R.W. Armstrong, F.J. Zerilli, in: *Tungsten and Tungsten Alloys—Recent Advances*, TMS, New Orleans, LA, 1991.
- [25] F.J. Zerilli, R.W. Armstrong, *J. Appl. Phys.* 61 (1987) 1816.
- [26] J.R. Klepaczko, C.Y. Chiem, *J. Mech. Phys. Solids* 34 (1986) 29.
- [27] D.J. Steinberg, S.G. Cochran, N.W. Guinan, *J. Appl. Phys.* 51 (1980) 3.
- [28] G. R. Johnson and W. H. Cook, in *7th Int. Symp. On Ballistics*, KIVI, The Hague, Netherlands, 1983, 541.
- [29] G.R. Johnson, W.H. Cook, *Eng. Fracture Mech.* 21 (1) (1985) 31.